An Efficiency-Optimized Control Strategy for Variable Flux Machines

Santiago Cianca Sosa
Institute of Electrical Engineering (ETI)
Karlsruhe Institute of Technology
Karlsruhe, Germany
santiago.cianca@student.kit.edu

Julius Kesten
Institute of Electrical Engineering (ETI)
Karlsruhe Institute of Technology
Karlsruhe, Germany
julius.kesten@kit.edu

Matthias Brodatzki
Institute of Electrical Engineering (ETI)
Karlsruhe Institute of Technology
Karlsruhe, Germany
brodatzki@kit.edu

Martin Doppelbauer
Institute of Electrical Engineering (ETI)
Karlsruhe Institute of Technology
Karlsruhe, Germany
martin.doppelbauer@kit.edu

***Abstract*—Variable flux machines enable online adjustment of the permanent magnet flux linkage, introducing an additional degree of freedom for efficiency-oriented control. This capability requires a coordinated treatment of operational efficiency and the energetic cost of MS manipulation.**
A state-based control structure is proposed that switches between standard operation and an efficiency optimizing decision mode. MS adjustments are executed through online-generated current trajectories that maintain torque while respecting voltage constraints. The decision logic relies on an amortization-time criterion: an MS change is only carried out if its energetic benefit is expected to outweigh the associated manipulation losses within a predefined horizon.
The proposed control strategy was evaluated on a WLTP driving segment, demonstrating that the method consistently selects locally advantageous MS levels and yields measurable efficiency improvements without compromising torque control.

***Index Terms*—variable flux machine, online magnetization control, torque-invariant current trajectory design, efficiency optimization**

I. Introduction

A. Variable flux machines' magnetization control

Permanent Magnet Synchronous Machines (PSMs), known for their high efficiency and power density [1], have become a preferred choice for traction applications [2]. The induced voltage in conventional PSMs with constant rotor excitation increases linearly with rotational speed, making field weakening necessary to reduce back-EMF and achieve an extended speed range. This operating mode incurs increased copper losses. Motivated by these limitations, variable flux machines (VFMs) have emerged as an alternative to traditional PSMs [3]–[5]. VFMs employ low-coercivity magnets, such as AlNiCo, which allow deliberate manipulation of the magnetization state (MS) during operation. As a result, the required armature current during field weakening decreases, offering potential efficiency gains [6].

The electrical model of the VFM is described by the voltage equations (1) and (2), where Ψ_d and Ψ_q denote the direct and quadrature axis flux linkages respectively [7]. Ψ_d consists of the direct flux linkage due to current excitation $\Psi_{\mathrm{d,el}}$ and that induced by the permanent magnets Ψ_PM.

$$u_\mathrm{d} = R_\mathrm{s}\, i_\mathrm{d} + \frac{\partial\, \Psi_{\mathrm{d,el}}}{\partial t} + \frac{\partial\, \Psi_\mathrm{PM}}{\partial t} - \omega_\mathrm{el}\, \Psi_\mathrm{q} \tag{1}$$

$$u_\mathrm{q} = R_\mathrm{s} i_\mathrm{q} + \frac{\partial\, \Psi_\mathrm{q}}{\partial t} + \omega_\mathrm{el}\, \Psi_\mathrm{d}, \tag{2}$$

where $\Psi_i = f(t, i, \Psi_\mathrm{rel})$ (see (4)). The torque produced by the VFM is calculated identically to the conventional PSM (3).

$$T_\mathrm{i} = \frac{3}{2}\, p\, (\Psi_\mathrm{d}\, i_\mathrm{q} - \Psi_\mathrm{q}\, i_\mathrm{d}) \tag{3}$$

Finally, the MS describes the permanent magnet flux linkage relative to its maximum possible value, as shown in (4).

$$\Psi_\mathrm{rel} = \frac{\Psi_\mathrm{PM}}{\Psi_\mathrm{PM,max}} \cdot 100\% \tag{4}$$

Applying short armature current trajectories enables the manipulation of the flux linkages and, correspondingly, the MS [8]. The MS primarily changes in response to i_d, with negative values leading to demagnetization, as shown in Fig. 1, and positive values resulting in re-magnetization. Cross saturation leads to a dependence of i_q.

The course of a demagnetization trajectory can be understood by examining its three consecutive phases [9]:

1) **Excitation:** $i_\mathrm{d,start}$ is continuously decreased to $i_\mathrm{d,demag}$.
2) **Hold:** $i_\mathrm{d,demag}$ is maintained for $\frac{1}{6}$ of the electrical period to ensure complete demagnetization of the permanent magnets [9].
3) **Recoil:** After the demagnetization process is complete, i_d is increased to $i_\mathrm{d,recoil}$.

The three phases are represented by the corresponding numbers ①-③ in both Fig. 2 and Fig. 4.

Once the demagnetization trajectory is completed, applying any current pair within the region bounded by the target MS

© 2026 IEEE. Personal use of this material is permitted. Permission from IEEE must be obtained for all other uses, in any current or future media, including reprinting/republishing this material for advertising or promotional purposes, creating new collective works, for resale or redistribution to servers or lists, or reuse of any copyrighted component of this work in other works.

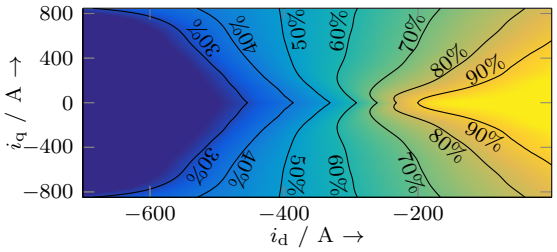
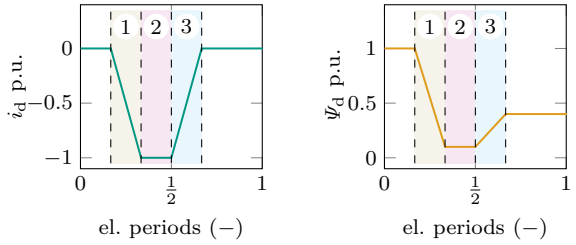


Fig. 1: Variation of the relative magnetization state Ψ_{rel} from 25% to 100% as a function of the current components i_{d} and i_{q} of the VFM analyzed in this study.



(a) d-current ramp (b) d-flux linkage

Fig. 2: Demagnetization process, schematic representation with the d-axis current ramp applied (a) and the resulting behaviour of the d-axis flux linkage (b).

contour and the quadrature axis does not further alter the MS. This behavior is known as the memory effect [4]. Re-magnetization trajectories follow the same phases. The main difference is that $i_{\mathrm{d,demag}}$ has a positive value.

Existing work employs a variety of current trajectory shapes and slew rates for MS manipulation. Trapezoidal profiles are commonly used, as in [10], [11], with reported slew rates ranging from 0.5 to 1.25 $\mathrm{A\,ms^{-1}}$. The authors of [12] demonstrated that sinusoidal trajectories can improve current tracking performance compared to trapezoidal profiles, albeit without explicitly enforcing a slew rate. Further, a two-phase dynamic trajectory formulation was proposed in [12], in which the slew rate is adapted online to exploit the available voltage reserve, achieving average slopes of approximately 12.38 $\mathrm{A\,ms^{-1}}$ while maintaining acceptable tracking quality.

Complementing these operational insights, a novel MTPA-derived approach for determining the efficiency map of VFMs considering relative magnetization was proposed in [13]. In this algorithm, Ψ_{rel}, i_{d}, and i_{q} are treated simultaneously as optimization variables in a single integrated calculation.

The current state of research provides a comprehensive foundation for deliberate MS manipulation and tracking [14] and offers an algorithmic framework for determining optimal operating points of VFMs. However, no prior work has addressed the conceptualization of an online efficiency-optimized strategy for MS manipulation in traction applications.

B. Contributions of This Study

The present study proposes an online operating point selection approach that determines the optimal MS based solely on the instantaneous torque and speed demand of an electric vehicle. The method operates without relying on additional external data that might allow a forecast of the expected load. Further, it explicitly rather than implicitly accounts for the voltage limit constraint during MS manipulation, through online calculation during the MS change. This study aims to design fast current trajectories that minimize torque fluctuations. A novel efficiency-optimized control strategy is introduced that evaluates additional losses associated with manipulation trajectories. Operating points are selected based on loss-amortization times relative to a defined decision interval

Section II presents the simulation model of the automotive drivetrain and its components. Section III introduces the model-based data, methodology, and design approach of the trajectory courses. Section IV describes the logical steps of the control strategy used to select the next magnetization state and outlines the simulation setup employed to validate the proposed loss amortization based approach. Section V presents the simulation results. Section VI concludes with a summary and outlook.

II. Electric Vehicle Simulation Model

The proposed control strategy was implemented in a *Simulink* model of an electric vehicle drivetrain, presented in Fig. 3. The model is based on a *Simulink* based tool for drive train modelling developed at the Institute of Electrical Engineering.

The core of the drivetrain model in Fig. 3 is the VFM (d). Its direct and quadrature axis voltages are computed using (1) and (2), while the MS is obtained from precomputed maps $\Psi_{\mathrm{rel}}(i_{\mathrm{d}}, i_{\mathrm{q}})$, as presented for the demagnetization in Fig. 1. Similar maps are employed for the re-magnetization. The electromagnetic torque is calculated using (3).

Regulation of the currents is handled by the motor control unit (MCU) (b), which employs field-oriented control with independent PI controllers for i_{d} and i_{q} respectively.

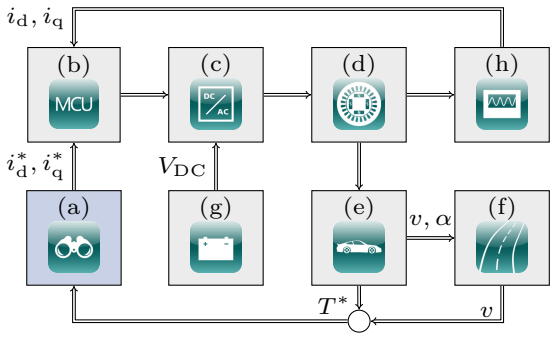


Fig. 3: Schematic *Simulink* model of an electric vehicle drivetrain.

Furthermore, clamping anti-windup was employed. Inductive terms in (1) and (2) are treated as additive disturbances, while the armature flux linkages are approximated from differential inductances to enable feedforward compensation. Current measurements i_d and i_q from sensor (h) are supplied to the MCU, and the drivetrain is powered by the ideal voltage source (g) and the lossless inverter (c).

Mechanical behavior, from rotor torque and speed transmission to the driving surface, is represented in components (d) and (e). The model incorporates external forces, internal losses, and mechanical transmission ratios. Component (f) provides the velocity v and inclination α profiles of driving cycles (e.g. standardized cycles like WLTP or NEDC, individual cycles can be supplied as well). The torque demand T^* is computed from the mechanical model based on the instantaneous cycle velocity and inclination.

Finally, the target value generator (a) was developed as part of this study. It selects the operating mode and provides the reference values for the currents i_{d^*} and i_{q^*} to the MCU. The efficiency-optimized control strategy is integrated into the setpoint generator and is discussed in detail in Section IV.

III. Current Trajectory Design

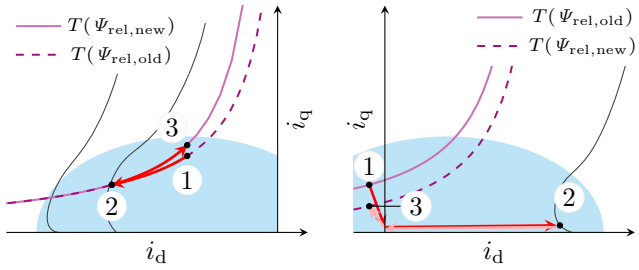
Magnetization trajectories define the transient evolution of the dq currents during MS manipulation, as shown in Fig. 2. The current waypoints are determined online and are subject to operating requirements:

- **(R1)** Overshoot in the MS change must be avoided: $|\Psi_{\mathrm{rel,goal}} - \Psi_{\mathrm{rel,goal}}{}^*| \leq \Delta\Psi_{\mathrm{rel,max}} = 5\%$.
- **(R2)** The torque should remain as constant as technically feasible throughout the MS-change process.
- **(R3)** The maximum voltage u_max (set to 90% of the nominal inverter limit $u_{\mathrm{max,inv}}$) must not be exceeded at any time, including voltage ripple.

The dataset is constructed using discrete MS levels with a fixed resolution. For each level, the corresponding torque hyperbola is derived from the torque equation (3), represented by the purple lines in Fig. 4, ensuring compliance with (R2). The current grid is sampled with a suffienctly fine grid as well, to allow obtaining intermediate points via linear interpolation. Voltage compliance during the hold phase is assessed by pre-estimating the expected envelope voltage in accordance with (R3). For this purpose, equations (1) and (2) are rewritten using differential inductances to express the time derivatives of Ψ_d and Ψ_q, while $\frac{d\Psi_\mathrm{PM}}{dt}$ is assumed negligible. The required differential inductances are extracted from simulation data. To capture ripple-induced variations in the currents, the corresponding envelope voltage expressions (5) and (6) are defined as follows:

$$u_{\mathrm{d,env}} = |R_\mathrm{s} i_\mathrm{d} - \omega_\mathrm{el}\,\Psi_\mathrm{q}| + \left|L_\mathrm{dd}\frac{\mathrm{d}i_\mathrm{d}}{\mathrm{d}t}\right| + \left|L_\mathrm{dq}\frac{\mathrm{d}i_\mathrm{q}}{\mathrm{d}t}\right| \quad (5)$$

$$u_{\mathrm{q,env}} = |R_\mathrm{s} i_\mathrm{q} + \omega_\mathrm{el}\,\Psi_\mathrm{d}| + \left|L_\mathrm{qd}\frac{\mathrm{d}i_\mathrm{d}}{\mathrm{d}t}\right| + \left|L_\mathrm{qq}\frac{\mathrm{d}i_\mathrm{q}}{\mathrm{d}t}\right| \quad (6)$$



(a) Demagnetization (b) Re-Magnetization

Fig. 4: Schematic representation of the demagnetization and re-magnetization path along torque hyperbolas (purple lines), envelope voltage ellipses (blue) and MS-contours (black lines).

The voltage envelopes are represented as blue ellipses in Fig 4.

A. Demagnetization Trajectories

The path of a demagnetization trajectory starts at $i_{\mathrm{d,start}}$ (step ① in Fig. 4a), and the target value $i_{\mathrm{d,demag}}$ (step ②) ideally corresponds to the intersection of the demagnetization contour of the target MS $\Psi_{\mathrm{rel,goal}}$ with the torque hyperbola of the current state $\Psi_{\mathrm{rel,old}}$. This intersection is represented by step ② in Fig. 4a: It is placed at the intersection point of $T(\Psi_{\mathrm{rel,old}})$ with the MS , given in dark grey. After the hold phase, i_d is returned to the operating point marked ③ on the torque hyperbola $T(\Psi_{\mathrm{rel,new}})$, reaching $i_{\mathrm{d,recoil}}$ according to section I-A. This is valid for cases where the voltage constraint is satisfied. Otherwise, the intersection point between the target MS contour and the envelope voltage ellipse is used.

During the excitation phase, i_d is continuously decreased to $i_{\mathrm{d,demag}}$, following a sinusoidal speed profile along the d-axis to achieve improved current-tracking performance and thus reduced torque pulsations, as shown in Fig. 5. The corresponding i_q trajectory is obtained by evaluating the torque hyperbola of the initial MS at each instantaneous value of i_d. After the hold phase, the recoil phase begins, during which i_d is increased again while i_q transitions to the torque hyperbola associated with the new MS.

A fixed sinusoidal transient reference with amplitude $\Delta I_\mathrm{ref} = 160\,\mathrm{A}$ and time period $T_\mathrm{ref} = 30\,\mathrm{ms}$ is used to define the shape of the excitation and recoil flanks. This reference profile provides a suitable compromise with respect to the design criteria and yields an average slew rate of $21.33\,\mathrm{A\,ms^{-1}}$ per flank. To preserve identical curvature and thus consistent dynamic behaviour for different amplitudes, the period is scaled proportionally according to (7).

$$T_\mathrm{traj} = T_\mathrm{ref}\sqrt{\frac{\Delta I}{\Delta I_\mathrm{ref}}} \quad (7)$$

This sinusoidal time profile serves as the reference speed profile for all demagnetization and re-magnetization transients.

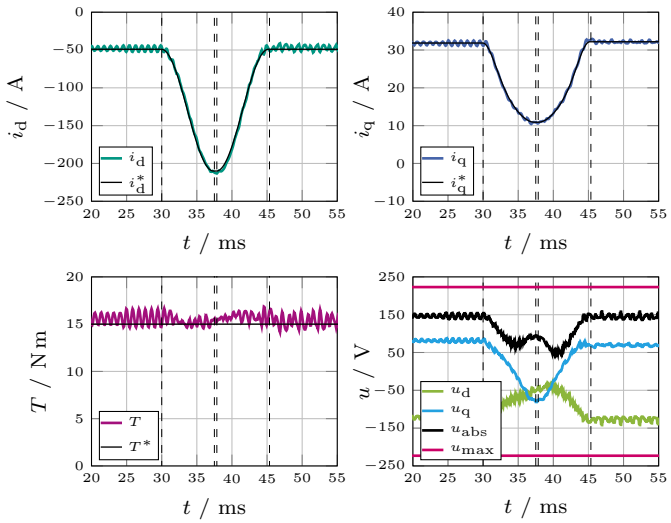


Fig. 5: Time evolution of current, torque, and voltage during the demagnetization trajectory at $7500\,\mathrm{min}^{-1}$.

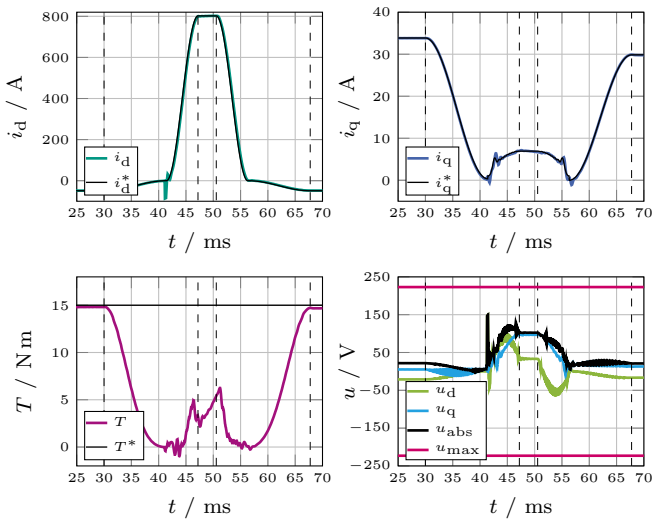


Fig. 6: Time evolution of current, torque, and voltage during the remagnetization trajectory at $1200\,\mathrm{min}^{-1}$.

Fig. 5 shows a small overshoot of i_d during the hold phase. The resulting over-demagnetization equals 0.7%, ensuring that constraint (R1) is fulfilled. Fig. 5c) confirms that constraint (R2) is met, while Fig. 5d) demonstrates compliance with constraint (R3).

B. Re-Magnetization Trajectories

The torque hyperbolas are discontinuous in the dq plane, diverging asymptotically for small positive i_d values. Consequently, no continuous torque-invariant path exists between $i_\mathrm{d,start}$ and the target MS contour. A direct transition between hyperbolas at the asymptote would induce severe torque pulsations. Therefore, the approach selected in this work is to temporarily reduce the torque to $0\,\mathrm{N\,m}$ and maintain it while i_d remains positive. Under these conditions, constraint (R2) cannot be fulfilled.

All i_q values corresponding to $0\,\mathrm{N\,m}$ torque in the first quadrant of the dq plane form an approximately linear relationship with a slightly positive slope. This line is hereafter referred to as the $0\,\mathrm{N\,m}$ line.

Fig. 4b illustrates the course of a re-magnetization trajectory as described above. Prior to execution, compliance with the voltage constraint (R3) is verified by estimating the envelope voltage along the $\Psi_\mathrm{rel,goal}$ contour. The trajectory begins at $i_\mathrm{d,start}$ and its corresponding i_q value on the current torque hyperbola (step ①). Subsequently, both i_d and i_q are reduced to $0\,\mathrm{A}$. Next, i_d is increased and i_q follows the $0\,\mathrm{N\,m}$ line until the intersection point with the target MS contour is reached (step ②). At this intersection, the current is held constant at $i_\mathrm{d,hold}$. During the recoil phase, i_d and i_q are decreased along the same path until reaching $i_\mathrm{d,recoil}$ and its corresponding $i_\mathrm{q,recoil}$ value on the torque hyperbola of $\Psi_\mathrm{rel,goal}$ (step ③).

All current flanks in Fig. 6 follow sinusoidal profiles to ensure smooth transitions between phases. The corresponding periods are calculated according to (7) and multiplied by 0.25 to shorten the overall manipulation time, which is possible for re-magnetization without endangering the stability of the process, whereas (7) was designed with regard to the demagnetization process, meaning any further reduction of the time period would make it unstable. This adjustment reduces losses, as the efficiency drops to nominally 0% while the system follows the $0\,\mathrm{N\,m}$ line.

Because small fluctuations in i_q have an increasingly pronounced effect on the torque at higher i_d levels, torque pulsations appear midway through the remagnetization process, as shown in Fig. 6c. In this case, i_d does not exhibit any overshoot during the hold phase, ensuring compliance with constraint (R1). Finally, the voltage remains below u_max throughout the trajectory, fulfilling constraint (R3).

IV. Control Strategy

The control strategy aims to maximize the efficiency of the simulated vehicle during driving cycles. Using the holistic efficiency map calculation algorithm for VFMs [13], the loss optimal currents (maximum torque per loss (MTPL)) $i_\mathrm{d,MTPL}$, $i_\mathrm{q,MTPL}$, and the corresponding optimal magnetization state $\Psi_\mathrm{rel,MTPL}$ were computed as functions of motor torque and speed. The resulting optimal MS distribution is shown in Fig. 7. This dataset enables the determination of the optimal current components and MS for any given torque T^* and rotational speed n^* demand defined by the driving cycle.

Inside the target value generator (Block a) in Fig. 3, the supervisory control layer is implemented as the state machine in Fig. 8. It governs the transitions between the four operating modes and executes the efficiency-optimized logic exclusively in the Decision state.

In the Normal operation state, the MS is held constant while the MTPL currents $i_\mathrm{d,MTPL}$ and $i_\mathrm{q,MTPL}$ are applied according to T^* and n^* and updated at the control frequency. At every decision interval Δt_d, the state machine enters

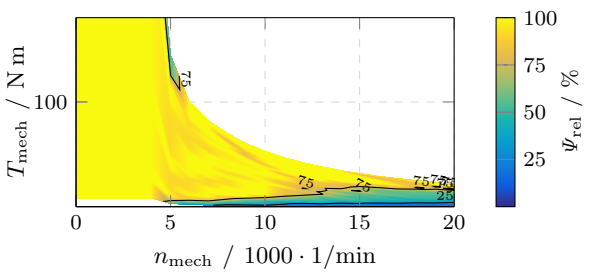


Fig. 7: Efficiency optimal Ψ_{rel} of the investigated machine.

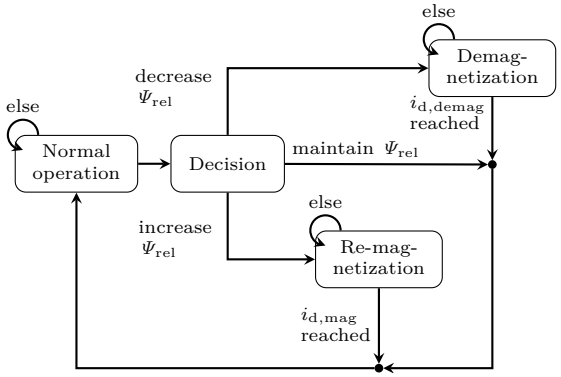


Fig. 8: Supervisory control layer state machine

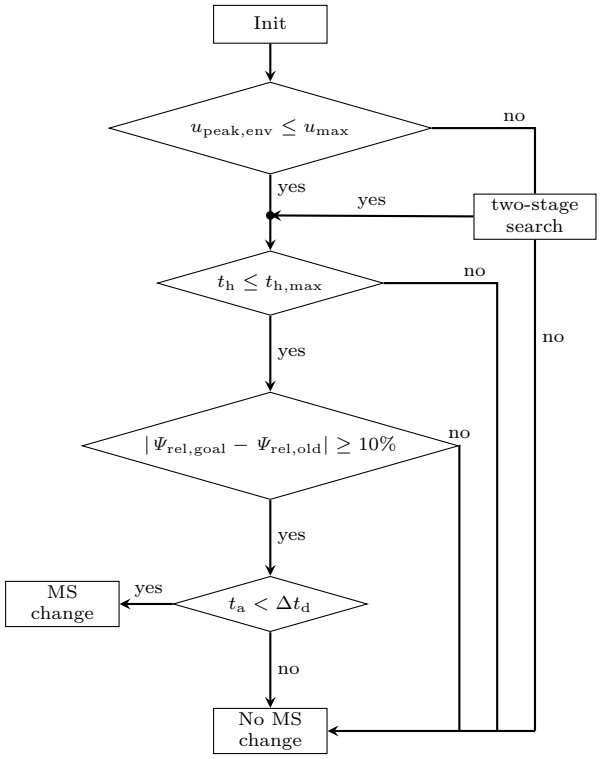


Fig. 9: Transition decision state machine.

the Decision state, where the efficiency-optimized logic is executed. If no MS adjustment is required, the system returns to the Normal operation state; otherwise, a re- or demagnetization trajectory is initiated.

A. Decision Logic

The five-step decision algorithm illustrated in Fig. 9 is employed to identify the target MS $\Psi_{\mathrm{rel,goal}}$ and assess, whether a transition is admissible.

Step one retrieves $\Psi_{\mathrm{rel,MTPL}}$ from Fig. 7. Step two verifies compliance with the voltage restriction (R3). As $|i_{\mathrm{d}}|$ increases during the final part of the excitation phase and throughout the hold phase, the required voltage rises, particularly when the target MS $\Psi_{\mathrm{rel,goal}}$ lies far from the current MS $\Psi_{\mathrm{rel,old}}$. To assess feasibility, the peak envelope voltage during the hold phase, $u_{\mathrm{peak,env}}$, is estimated using (5) and (6) and compared with u_{max}. If the initial hyperbola–contour-intersection is voltage-compliant (i.e. if $u_{\mathrm{peak,env}} \leq u_{\mathrm{max}}$ holds), it is selected as the hold point $(i_{\mathrm{d,demag}}, i_{\mathrm{q,demag}})$. If $u_{\mathrm{peak,env}} > u_{\mathrm{max}}$, the algorithm performs a two-stage search for an admissible MS. First, MS closer to the current one are examined to identify the nearest operating point that intersects the envelope-voltage ellipse. Once a suitable Ψ_{rel} is found, the algorithm moves along its contour starting from $i_{\mathrm{d}} = 0$ toward higher $|i_{\mathrm{d}}|$ values until the first intersection with the envelope voltage ellipse is encountered; this point is then chosen as $(i_{\mathrm{d,demag}}, i_{\mathrm{q,demag}})$.

Step three evaluates the duration of the hold phase. Since its duration corresponds to $1/6$ of the electrical period, it increases sharply as the rotational speed decreases and theoretically diverges at standstill. To prevent excessive manipulation losses, the hold phase is capped at a given maximum $t_{\mathrm{h,max}} = 10\,\mathrm{ms}$. For operating speeds below the limit corresponding to $t_{\mathrm{h,max}}$, MS manipulation is still executed, but the hold phase is fixed to this maximum duration.

Step four enforces a minimum MS change, requiring $\Psi_{\mathrm{rel,goal}} - \Psi_{\mathrm{rel,old}} \geq \Delta\Psi_{\mathrm{rel,min}}$ (10%) to avoid dithering and improve consistency.

Step five performs an efficiency-based evaluation using the amortization time t_{a}.

B. Amortization time based evaluation

Future load and speed profiles are unknown in real driving conditions, so a global optimization over time is not feasible. The control strategy employs local optimization between consecutive decision intervals. An MS manipulation is initiated only if the amortization time t_a is shorter than the decision interval Δt_{d}, which simultaneously acts as the threshold for admissible MS transitions.

The amortization time t_{a} defines the minimum operating duration in the new magnetization state $\Psi_{\mathrm{rel,goal}}$ after which the additional energy losses caused by the MS manipulation process are compensated by the improved efficiency of this new state. It is derived from the energetic balance between

the efficiencies in the current and target magnetization states, including the transient losses along the current trajectory:

$$\eta_\mathrm{t} \cdot \Delta t_\mathrm{t} + \eta_\mathrm{MS,goal} \cdot (t_\mathrm{a} - \Delta t_\mathrm{t}) = \eta_\mathrm{MS,old} \cdot t_\mathrm{a} \tag{8}$$

Here, η_t denotes the mean efficiency during the magnetization trajectory of duration Δt_t, while $\eta_\mathrm{MS,old}$ and $\eta_\mathrm{MS,goal}$ represent the steady-state efficiencies in the current and target magnetization states, respectively.

The total loss power P_l comprises the electromagnetic losses; namely copper, iron, and magnet losses, which were pre-determined from FEM simulations as functions of i_d, i_q, and Ψ_rel. Further loss components such as AC copper loss or inverter induced losses are not considered here, because the data was not available. However, the presented methodology allows integration of these loss components. If available, the corresponding loss maps are supplied to the algorithm along the existing data, resulting in different optima; the operating principle remains unchanged. The mechanical output power corresponding to the current operating point (M^*, n^*) is used to compute the efficiency η. Trajectory losses $P_\mathrm{l,t}$ are obtained by evaluating the electromagnetic losses along the discrete current trajectory and averaging them over Δt_t to yield η_t.

V. Results

The proposed manipulation trajectory, which follows torque hyperbolas and employs sinusoidal flank profiles, enables torque-invariant demagnetizations. Owing to the discontinuity of the torque hyperbolas in the positive i_d quadrant, re-magnetization enforcing $T = 0\,\mathrm{N\,m}$ is employed. The field-oriented control exhibits sufficiently low tracking errors such that the MS overshoot remains below the acceptable 5% limit, thereby fulfilling requirement (R1). Although the resulting slew rates are lower than the voltage-maximizing approach of Chen [12], the sinusoidal flanks provide excellent current-tracking behaviour and curvature-invariant scalability with respect to the current amplitude. As shown in Fig. 10, the proposed method achieves manipulation speeds that are between 31.2% and 35.8% slower for representative amplitudes, despite operating without online voltage maximization. Overall, the demagnetization trajectories satisfy requirements (R1)-(R3), whereas re-magnetization violates the torque requirement (R2).

The machine used in this work is presented in [14]. MS changes with this machine are comparably current demanding. Therefore, the results presented below are to be seen as a validation of the methodology introduced in this work, rather than final statements on the possible efficiency gains of VFM. The validation of the proposed efficiency-optimized control strategy is carried out by simulating the first 85 s of the WLTP extra-high-speed phase [15] using the drivetrain model presented in Fig. 3. This segment of the WLTP reaches the highest velocities of the cycle while requiring only moderate torque levels. One run applied the proposed control strategy, while the other disabled all MS manipulations. As indicated in Fig. 7, the investigated operating points lie in the lower-right

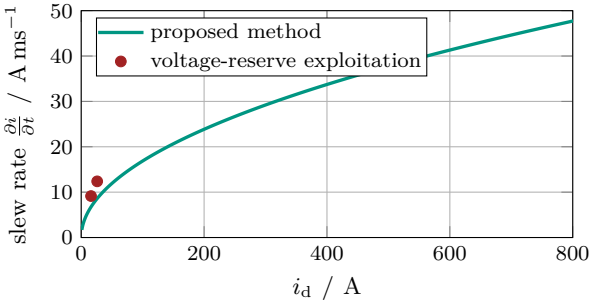


Fig. 10: Comparison of flank slew rates relative to the manipulation current amplitude for the proposed method (green) and the voltage-reserve exploitation technique presented in [12] (red).

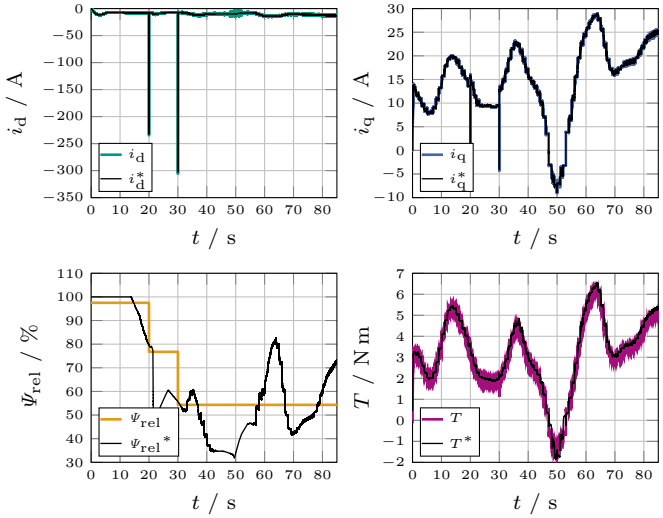


Fig. 11: Transient evolution of i_d, i_q, M, and Ψ_rel during the evaluated WLTP segment.

region of the $\Psi_\mathrm{rel,MTPL}$, where a reduced MS is energetically favourable.

The transient evolution of the currents, torque, and MS is shown in Fig. 11. With a decision interval of $\Delta t_\mathrm{d} = 10\,\mathrm{s}$, two demagnetization actions are triggered at $t = 20\,\mathrm{s}$ and $t = 30\,\mathrm{s}$, yielding amortization times of $t_\mathrm{a} = 5.36\,\mathrm{s}$ and $t_\mathrm{a} = 3.29\,\mathrm{s}$ respectively. Torque tracking remains accurate throughout, and the magnetization state reliably converges to the selected values at the decision instants while following the overall trend of the optimal $\Psi_\mathrm{rel,MTPL}$ trajectory.

Loss behavior and cumulative efficiency $\bar{\eta}$ development are depicted in Fig. 12. In the left diagram, the instantaneous loss power is depicted, where $P_\mathrm{l,MS}$ represents the values for an adaptive MS. $P_\mathrm{l,stat}$ represents the losses for the same machine without adjusting Ψ_rel. On the right side, the difference in cumulative efficiency $\Delta\bar{\eta}$ is plotted. With this value, the differences in efficiency of the machine with and without adaptive MS are compared, integrated over the cycle time introduced above. For the first 20 s, $\Delta\bar{\eta}$ is 0, since both

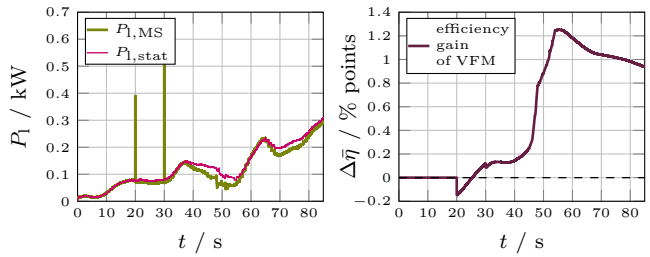


Fig. 12: Instantaneous loss evolution and the cumulative averaged efficiency difference obtained with the proposed strategy relative to the baseline.

machines operate with the same $\Psi_{\mathrm{rel}} = 100\,\%$. After the first demagnetization at $t = 20\,\mathrm{s}$, the instantaneous losses remain consistently below the baseline, except for a brief interval around $t \approx 60\,\mathrm{s}$ where $\Psi_{\mathrm{rel,MTPL}}$ temporarily increases (see Fig. 11). As a result, the cumulative efficiency difference rises steadily, peaking at roughly $1.25\,\%$ before settling at a still notable $0.94\,\%$ by the end of the evaluated window. The observed efficiency improvement is compatible with the $\Psi_{\mathrm{rel,MTPL}}$ distribution in Fig. 7, which favours lower MS levels at higher speeds and moderate torque. The amortization-based decision logic consequently triggers MS adjustments in operating points where a local energetic benefit can be expected.

VI. Conclusion and Outlook

A manipulation current trajectory design and an online magnetization control strategy for VFMs was introduced. The sinusoidal flank profiles and torque-hyperbola guidance enable torque-invariant demagnetization with good tracking performance and competitive manipulation times, without explicit voltage-reserve exploitation. A fundamental limitation is that any re-magnetization step breaks torque invariance.

An amortization-based decision logic was proposed to determine when an MS change is locally beneficial. Because it requires no preview information, the strategy is well suited for operating regimes with sustained high speed and moderate load, such as highway driving. The WLTP evaluation showed that it reliably selects energetically favourable MS levels and achieves measurable efficiency gains while maintaining stable torque behavior.

The present strategy relies exclusively on instantaneous operating conditions and therefore performs a purely local optimization. With access to external information - such as GPS data, traffic forecasts, or prior driving statistics - the controller could anticipate upcoming speed profiles and extend the optimization horizon. This would enable the transition from a locally optimal scheme to a global or longer horizon-based strategy that coordinates MS change decisions more effectively over time. Integrating such preview information, together with uncertainty handling and real-time constraints, represents a promising direction for future research on energy-optimized operation of VFMs.

In future work, a full cycle analysis is to be carried out with an adequately designed machine including a more sophisticated loss model, allowing the realization of the VFM's full potential. Subsequently, a machine prototype is to be built for metrological validation.

References

[1] C. Chan, K. Chau, J. Jiang, W. Xia, M. Zhu, and R. Zhang, "Novel permanent magnet motor drives for electric vehicles," *IEEE Transactions on Industrial Electronics*, vol. 43, pp. 331–339, Apr. 1996.

[2] K. Aiso and K. Akatsu, "Performance Comparison of High-Speed Motors for Electric Vehicle," *World Electric Vehicle Journal*, vol. 13, p. 57, Mar. 2022.

[3] V. Ostovic, "Memory motors," *IEEE Industry Applications Magazine*, vol. 9, pp. 52–61, Jan. 2003.

[4] K. Sakai, K. Yuki, Y. Hashiba, N. Takahashi, and K. Yasui, "Principle of the variable-magnetic-force memory motor," in *2009 International Conference on Electrical Machines and Systems*, pp. 1–6, Nov. 2009.

[5] Z. Zhou, H. Hua, and Z. Zhu, "Flux-Adjustable Permanent Magnet Machines in Traction Applications," *World Electric Vehicle Journal*, vol. 13, p. 60, Mar. 2022.

[6] S. Mishra and B. K. Nayak, "REVIEW ON MODELLING AND ANALYSIS OF VARIABLE FLUX MACHINES FOR TRACTION APPLICATION," *INTERNATIONAL JOURNAL OF ELECTRICAL ENGINEERING AND TECHNOLOGY*, vol. 11, Apr. 2020.

[7] B. Stumberger, G. Stumberger, D. Dolinar, A. Hamler, and M. Trlep, "Evaluation of saturation and cross-magnetization effects in interior permanent-magnet synchronous motor," *IEEE Transactions on Industry Applications*, vol. 39, pp. 1264–1271, Sept. 2003.

[8] J. Chen, J. Li, and R. Qu, "Analysis, Modeling, and Current Trajectory Control of Magnetization State Manipulation in Variable-Flux Permanent Magnet Machines," *IEEE Transactions on Industrial Electronics*, vol. 66, pp. 5133–5143, July 2019. Publisher: Institute of Electrical and Electronics Engineers (IEEE).

[9] M. S. Mirazimi, C. Chen, P. Pescetto, S. Ferrari, G. Pellegrino, M. Diana, and T. Thiringer, "Accurate Modeling of Variable- Flux PMSMs without Electromagnetic Co-Simulation," in *2024 International Symposium on Power Electronics, Electrical Drives, Automation and Motion (SPEEDAM)*, (Napoli, Italy), pp. 625–630, IEEE, June 2024.

[10] Y. Zhong, H. Lin, J. Wang, R. Tu, H. Yang, S. Lyu, and X. Liu, "Variable Time Magnetization Current Trajectory Control Method for Variable Flux Memory Machines," *IEEE Transactions on Transportation Electrification*, vol. 8, pp. 3100–3110, Sept. 2022.

[11] J. Chen, H. Fang, and R. Qu, "Online Magnetization Trajectory Prediction and Current Control for a Variable-Flux Permanent Magnet Machine," *IEEE Access*, vol. 8, pp. 41325–41334, 2020.

[12] Z. Chen, H. Lin, Y. Zhong, S. Lyu, and H. Yang, "A Novel Current Control Strategy for Magnetization State Manipulation of Variable Flux Memory Machine Based on Linear Active Disturbance Rejection," *IEEE Transactions on Power Electronics*, vol. 37, pp. 1962–1971, Feb. 2022.

[13] J. Kesten, P. Müller, M. Brodatzki, and M. Doppelbauer, "Holistic Efficiency Map Calculation of Variable Flux Machines Regarding Relative Magnetisation," in *2024 International Symposium on Power Electronics, Electrical Drives, Automation and Motion (SPEEDAM)*, (Napoli, Italy), pp. 1023–1029, IEEE, June 2024.

[14] S. Beck, J. Kesten, and M. Doppelbauer, "A Review on Flux Estimation Methods for Variable Flux Machine Applications," in *2025 Energy Conversion Congress & Expo Europe (ECCE Europe)*, (Birmingham, United Kingdom), pp. 1–6, IEEE, Sept. 2025.

[15] UNECE, "Global technical regulation no. 15 worldwide harmonized light vehicles test procedure," Tech. Rep. GTR No. 15, United Nations Economic Commission for Europe, Geneva, 2014.